Electron and phonon renormalization near charged defects in carbon nanotubes

INDHIRA O. MACIEL[1]*, NEIL ANDERSON[2]*†, MARCOS A. PIMENTA[1], ACHIM HARTSCHUH[3], HUIHONG QIAN[3], MAURICIO TERRONES[4], HUMBERTO TERRONES[4], JESSICA CAMPOS-DELGADO[4], APPARAO M. RAO[5], LUKAS NOVOTNY[2]‡ AND ADO JORIO[1,6]‡

[1]Departamento de Física, Universidade Federal de Minas Gerais, Belo Horizonte, MG, 30123-970, Brazil
[2]Institute of Optics and Department of Physics, University of Rochester, Rochester, New York 14627, USA
[3]Ludwig-Maximilians-Universität München, Department Chemie und Biochemie Physikalische Chemie and CeNS, München, 80539, Germany
[4]Advanced Materials Department, IPICYT, San Luis Potosí, SLP, 78216, Mexico
[5]Department of Physics and Astronomy and Center for Optical Materials Science and Engineering Technologies, Clemson University, Clemson, South Carolina 29621, USA
[6]Divisão de Metrologia de Materiais, Instituto Nacional de Metrologia, Normalização e Qualidade Industrial (INMETRO), Duque de Caxias, RJ, 25250-020, Brazil
*These authors contributed equally to this work
†Present address: Bausch & Lomb, 1400 N. Goodman St., Rochester, New York 14609, USA
‡e-mail: novotny@optics.rochester.edu; adojorio@fisica.ufmg.br

Published online: 19 October 2008; doi:10.1038/nmat2296

Owing to their influence on electrons and phonons, defects can significantly alter electrical conductance, and optical, mechanical and thermal properties of a material. Thus, understanding and control of defects, including dopants in low-dimensional systems, hold great promise for engineered materials and nanoscale devices. Here, we characterize experimentally the effects of a single defect on electrons and phonons in single-wall carbon nanotubes. The effects demonstrated here are unusual in that they are not caused by defect-induced symmetry breaking. Electrons and phonons are strongly coupled in sp^2 carbon systems, and a defect causes renormalization of electron and phonon energies. We find that near a negatively charged defect, the electron velocity is increased, which in turn influences lattice vibrations locally. Combining measurements on nanotube ensembles and on single nanotubes, we capture the relation between atomic response and the readily accessible macroscopic behaviour.

Interest in the fundamental and applied properties of sp^2-hybridized carbon nanomaterials such as nanotubes, nanohorns, nanoribbons and sheets centres on their unique structural, chemical, mechanical, thermal, optical, optoelectronic and electronic properties[1]. Electrons in graphene behave as massless Dirac fermions[2], exhibiting a linear dispersion near the Fermi level at the K point in the hexagonal Brillouin zone (upper panel of Fig. 1). Furthermore, electrons and phonons exhibit strong coupling in sp^2-hybridized carbon materials. The coupling generates a softening in the phonon dispersion at the K and Γ points, known as the Kohn anomalies (lower panel of Fig. 1)[3–5], and a breakdown of the adiabatic (Born–Oppenheimer) approximation[6], and therefore has important consequences for doping[7] and transport properties[1]. Now that the low-dimensional crystalline properties of carbon nanomaterials are relatively well understood, attention is turning increasingly to the study of defects in these materials, in particular in carbon nanotubes[1,8,9].

Spectroscopy, especially Raman scattering, has been largely used to study defects in sp^2 carbon materials,[10–13] including doping[7,14–16]. Defects usually break the selection rules, so that broadening and new peaks can be observed in the Raman spectra[10,11], mostly related to specific phonons in the interior of the Brillouin zone that are enhanced by double-resonance processes[12,13]. Besides usual symmetry breaking effects, the presence of charged defects will renormalize the energies of the strongly coupled electrons and phonons, as indicated in Fig. 1 by the dashed curves. Probing of the defect-induced renormalization of electrons and phonons locally, near the defect sites, is the subject of this work.

The so-called G′ band (see Fig. 2) is a well-known Raman-allowed second-order feature that is observed in the Raman spectra of all sp^2 carbon materials[10,11], interesting for being extremely sensitive to the π electronic structure. For example, this band has recently been used to study the electronic and vibrational structure in graphene samples depending on the number of layers[17–19], even though the interaction between layers is very weak. Figure 2 shows the G′ band in different sp^2 carbon materials. The three upper curves are for single-wall carbon nanotubes (SWNTs) prepared by different methods (see Methods for sample details). The upper plot is for heat-treated undoped SWNTs and shows a single G'_P peak (P for 'pristine') centred at $\omega_{G'_P} = 2{,}676\,\mathrm{cm}^{-1}$. On doping, a new G′ peak is observed at lower/higher frequency for n/p doping. The spectra of graphene, highly oriented pyrolytic graphite (HOPG) and amorphous carbon are also presented in Fig. 2 to clearly show that the new peak cannot be related to other forms of sp^2 carbon. This new peak, from now on called the G'_D peak (D for 'defect'), appears in the G′ spectra of doped SWNTs.

As a defect site is a structure localized at the atomic level, diffraction-limited optics (resolution $\sim \lambda/2 \geqslant 0.2\,\mu\mathrm{m}$) is not able to probe the real spatial scale associated with defect phenomena. To elucidate the true origin of the G'_D peak, we use near-field Raman

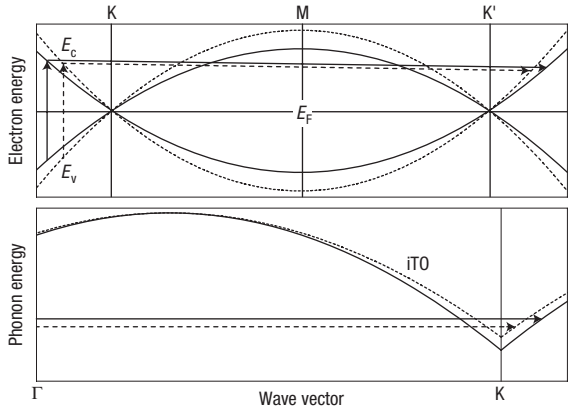

Figure 1 Schematic model showing the renormalization of electron and phonon energies near a negatively charged defect, and its influence on the double-resonance G′ scattering process discussed in this work. The upper panel shows the dispersion of the π and π^* electrons along the KMK′ direction in the hexagonal Brillouin zone, near the Fermi level (E_F). The lower panel shows the iTO phonon branch along the ΓK direction. The arrows in the upper panel indicate electron transitions by photon absorption (vertical arrows) and phonon scattering (nearly horizontal arrows). The arrows in the lower panel indicate the energies for the same phonons scattering electrons in the upper panel. Dashed lines represent the renormalized structure near the defect sites.

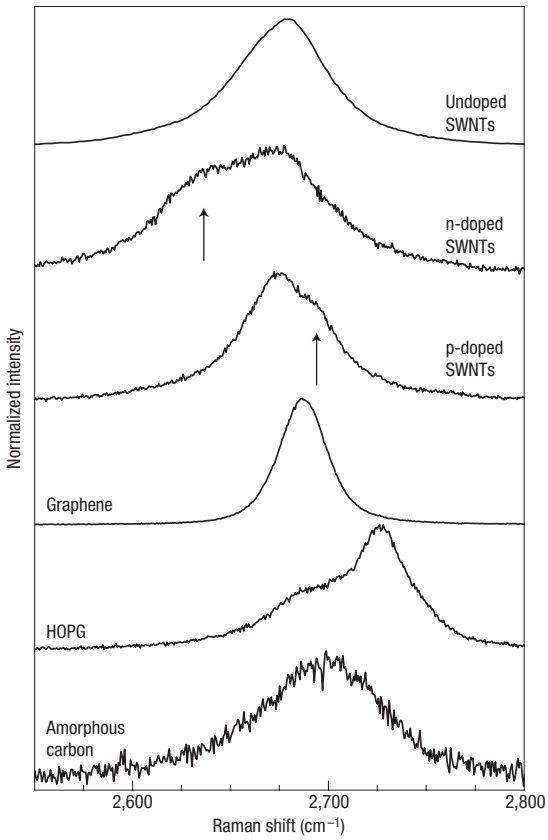

Figure 2 The G′ Raman band in different sp^2 carbon materials measured at room temperature with $E_{laser} = 2.41$ eV (514 nm). The arrows point to defect-induced peaks in the G′ for doped SWNTs. The p/n doping comes from substitutional boron/nitrogen atoms[15,16], the nearest neighbours of carbon in the periodic table. The spectra of graphene, HOPG and amorphous carbon are shown for comparison. See Methods for sample details.

and near-field photoluminescence imaging and spectroscopy to spatially resolve local defect states/sites along an individual SWNT (ref. 20). Figure 3a shows the photoluminescence spectra acquired from a (9, 1) SWNT. The (9, 1) structural (n, m) assignment[1] is based on determining the peak position of the emission spectra ($\lambda = 904$ nm) and the radial breathing mode ($\omega_{RBM} = 302$ cm^{-1}) in the corresponding Raman spectrum, shown in Fig. 3b. Figure 3c shows a near-field photoluminescence image of the (9, 1) SWNT, where the image contrast is provided by spectrally integrating over the photoluminescence peak centred at $\lambda = 904$ nm. The most striking feature in this image is the high degree of spatial localization of the photoluminescence emission along the SWNT. This is evident by inspection of the extended topography image of the nanotube shown in Fig. 3f, and also of the near-field Raman image of the tangential C–C stretching mode (named the G band, near 1,590 cm^{-1}) shown in Fig. 3d. Whereas from Fig. 3d we observe that the G band Raman scattering is present along the entire length of the nanotube, from Fig. 3e we observe increased symmetry-breaking defect-induced Raman scattering (D band, ~1,300 cm^{-1}) (refs 10–13) localized at the same region where photoluminescence was detected. Localized photoluminescence emission along single-wall carbon nanotubes is often observed in our near-field experiments, and it correlates with the local D band intensity, suggesting the existence of trapped excitons. Therefore, it is evident that bright photoluminescence emission, that is, exciton recombination, originates from a defect site along the SWNT. Once the defect site is located, we can monitor the G′ band and show that a clear change in the G′ line shape is measured near the defect site (see Fig. 3g), as expected.

The G′ band feature has been well characterized in the literature, and its frequency is known to depend both on excitation laser energy and tube diameter[21,22]. In our near-field experiment, with a $\lambda = 633$ nm laser, the G′ feature for the (9, 1) SWNT is expected to exhibit a single Lorentzian peak located at 2,613 cm^{-1} (refs 21,22). Although the G'_P peak is observed in excellent agreement with expectations ($\omega_{G'_P} = 2{,}610$ cm^{-1}), over the defective region, a new G'_D peak is observed (see asterisks in Fig. 3g), redshifted from the G'_P peak ($\omega_{G'_D} = 2{,}591$ cm^{-1}). The localized character of the G'_D scattering process is thus established.

Besides the p/n charge signal effect (shown in Fig. 2) and the localized emission (shown in Fig. 3), for a deeper understanding of the physics behind the defect-induced G'_D band, we analyse the dependence of the G′ peaks on the excitation laser energy (E_{laser}), as shown in Fig. 4a. The evolution of the G′ peak frequencies $\omega_{G'_P}$ and $\omega_{G'_D}$ for n-doped SWNTs are plotted in Fig. 4b, and fitted with a linear relation

$$\omega_{G'} = AE_{laser} + B. \quad (1)$$

For the defect-induced G'_D peak, the value of A is smaller and the value of B is larger when compared with the corresponding values for the G'_P peak (see caption to Fig. 4 for A and B values). These changes reveal the renormalization effect caused by the negatively charged defect on the local electronic and vibrational structure, as discussed below.

The second-order symmetry-allowed G′ Raman scattering process occurs in all sp^2 carbon materials, involving in-plane transversal optical (iTO) phonons near the K point in the hexagonal Brillouin zone, selected by the double-resonance process[10–13]. An excited electron with wave vector **k** resonantly

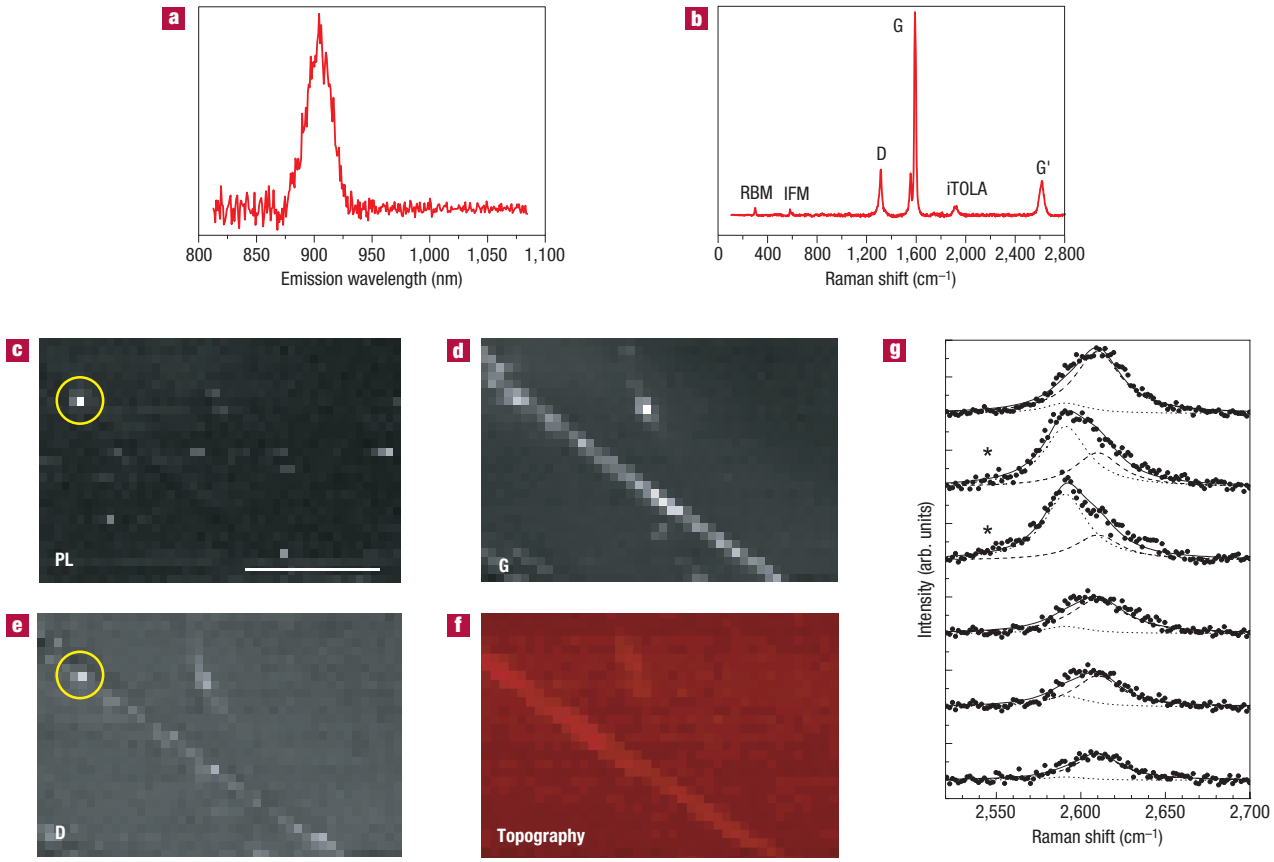

Figure 3 Near-field Raman and photoluminescence spectroscopy and imaging of a (9, 1) SWNT with $E_{laser} = 1.96$ eV (633 nm). a, Photoluminescence emission at $\lambda = 904$ nm. **b**, Raman spectrum. The Raman features are labelled[21]. **c**, Near-field photoluminescence image of the SWNT revealing localized excitonic emission. The scale bar denotes 250 nm. **d**,**e**, Near-field Raman imaging of the same SWNT, where the image contrast is provided by spectrally integrating over the tangential G (**d**) and defect-induced D bands (**e**). **f**, Corresponding topography image. **g**, Evolution of the G′ band spectra near the defective segment of the (9, 1) SWNT. The spectra were taken in steps of 25 nm along the nanotube, showing the defect-induced G'_D peak (dotted Lorentzian). The asterisks denote the spatial locations where localized photoluminescence and defect-induced D band scattering were measured (see yellow circles in **c** and **e**, respectively). The $\omega_{G'_P} - \omega_{G'_D}$ splitting observed in **g** is smaller than the splitting observed in the second (from the top) spectrum in Fig. 2 because the spectra were measured with different excitation laser energies, as discussed in the text.

selects a phonon with wave vector $\mathbf{q} \approx -2\mathbf{k}$ (refs 12,13,23). When considering one-dimensional nanotubes, momentum conservation for electron–phonon interaction requires that both linear and angular momenta are preserved. In the zone-folding picture, this is similar to two-dimensional linear momentum conservation in graphene[23]. Therefore, the graphene picture can be transferred to carbon nanotubes, and it will be used here because it is more didactic and general for sp^2 carbons. This relation between $\mathbf{k}$ and $\mathbf{q}$, together with the Dirac–Fermion behaviour for high-speed electrons ($v_F = c/300$, where v_F is the Fermi velocity and c is the speed of light)[2] and the Kohn anomaly for phonons[3], makes the G′ band strongly dependent on the particular electronic structure.

The linear dispersion for electrons has been broadly used to explain the frequencies of many dispersive features in the Raman spectra of undoped sp^2 carbon materials[10–13]. The excited electron with wave vector of modulus k is generated by resonance with the excitation laser[12,13]

$$E_{laser} = E_c - E_v = 2\hbar v_F k \approx \hbar v_F q, \qquad (2)$$

where the subscripts v and c stand for valence and conduction bands, respectively. Changing E_{laser} changes k linearly, and consequently q, so that the electronic structure can be probed using phonon measurements[12,13,17–19]. A schematic model showing the defect-induced renormalization of electron and phonon energies and its influence on the double-resonance G′ scattering process is shown in Fig. 1. The two resonant processes, the optical absorption and the scattering of the excited electron by a phonon, are represented by the vertical and nearly horizontal arrows, respectively. The G'_P follows the unperturbed process (solid lines), whereas the G'_D follows the process where electron and phonon energies are renormalized (dashed lines). The G′ phonon wave vector q connecting the two excited electronic states (nearly horizontal arrows) is selected by E_{laser} (vertical arrows), according to equation (2). Considering a linear dispersion, the constant B in equation (1) gives the G′ frequency at the K point, and the increase in B near the defect location is a direct measure of the hardening of the iTO phonon branch at the K point, due to the renormalization of the phonon energies[3,4] near the defect site. Phonon renormalization has been observed recently for the tangential G band ($\sim$1,580 cm^{-1}) in SWNT-based[5] and graphene-based[6] transport devices, although under different experimental conditions, that is, on gate-induced doping. The gate doping experiments on single-[24] and bi-layer[25] graphene and on carbon nanotubes[26] show a G′ frequency behaviour that is in quantitative agreement with our findings, indicating that the

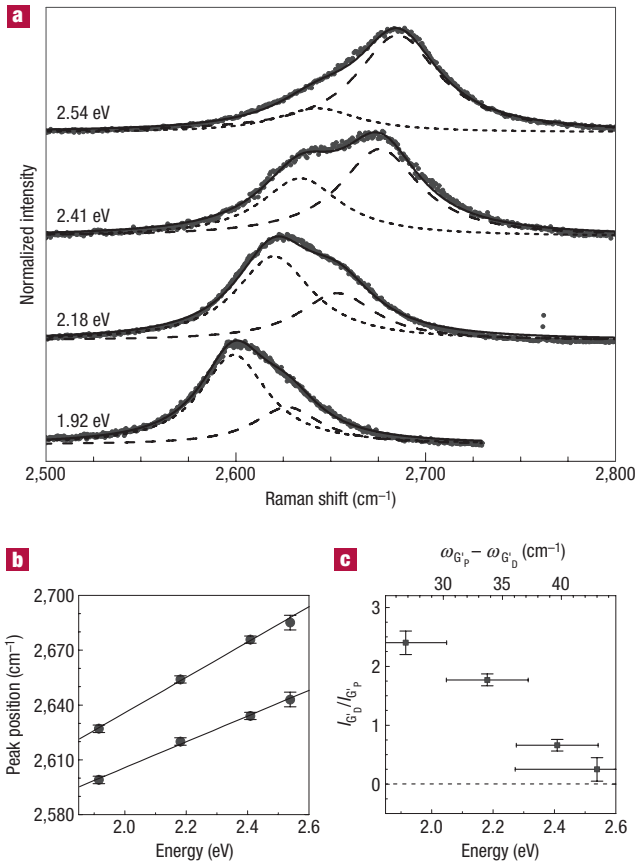

Figure 4 Dependence of the G′ band on E_{laser} for the n-doped SWNT sample. **a**, The G′ band spectra with different E_{laser}. **b**, The peak position as a function of E_{laser}, obtained by fitting the spectra in **a** with two Lorentzians. The error bars show the uncertainty in frequency definition. Common full-width at half-maximums are used, and the values increase linearly with E_{laser}, from $\Gamma = 43$ to 53 cm^{-1}. The solid lines are linear fits (see equation (1)), giving $\omega_{G'_P} = (97 \pm 5)E_{laser} + (2{,}442 \pm 11)$ and $\omega_{G'_D} = (71 \pm 4)E_{laser} + (2{,}465 \pm 11)$. **c**, G′ intensity ratio ($I_{G'_D}/I_{G'_P}$) as a function of E_{laser}. The vertical error bars show the uncertainty in $I_{G'_D}/I_{G'_P}$. The horizontal error bars show the uncertainty in the frequency splitting $\omega_{G'_P} - \omega_{G'_D} = 26E_{laser} - 23$, which is shown on the upper axis.

effect observed here for chemically doped SWNTs can be broadly applied to doping of sp^2-hybridized carbon materials in general. To explain the G'_D behaviour observed in Fig. 4, the phonon hardening indicated by the constant B alone is not sufficient; otherwise the defect-induced G'_D peak would always be observed at a higher frequency than the G'_P peak. The observation of G'_D at the lower frequency side is due to the weaker dependence of G'_D on E_{laser}, given by the parameter A in equation (1). The smaller value of the dispersion coefficient A is a measure of the renormalization of the phonon and electron energies near the K point ($A = v_q/v_F$, where v_q is the slope of the iTO phonon branch near K), the defect causing a change in the Fermi velocity v_F as well. Although the defect increases the phonon energies by reducing the phonon branch slope v_q near the K point (dashed curve in the lower panel of Fig. 1), the increase in the electronic Fermi velocity v_F (dashed curves in the upper panel) causes the double-resonance process to select a lower frequency phonon (dashed arrow in the lower panel) and exhibit a smaller dispersion with E_{laser}, as observed in Fig. 4. Therefore, the data in Fig. 4 indicate that electrons near a negatively charged defect site actually have higher energies, that is, higher speed v_F than its unperturbed counterpart.

Electron and phonon renormalization under doping is expected from theory[24,27–30]. Das *et al.*[24] carried out first-principles calculations to study the iTO frequency changes related to the optimization of the lattice parameters in gate-doped graphene. They considered that the G′ phonons are too far away from the K point to suffer the effects of the Kohn anomaly. Although their calculations are in qualitative agreement with our observations, showing a G′ asymmetric redshift versus blueshift for n- versus p-gate doping, the predicted shifts are much smaller than the experimental values, confirming that phonon renormalization alone cannot explain the G′ doping behaviour. Phonon renormalization due to non-local exchange-correlation effects was also demonstrated theoretically[27]. Electron renormalization under doping is expected theoretically due to many different effects, such as disorder in the electron hopping[28] and several many-body interactions, including non-Fermi liquid behaviour[29] and electron–phonon coupling renormalizing the electronic energies[30]. As the many-body corrections generally give a negative renormalization to the electronic energies, independent of doping sign[29,30], our data indicate that the most important effect for electron renormalization is the changes in the value of the hopping amplitude caused by lattice distortion[28]. The connection between the local lattice distortions[28] and the double-resonance model based on energy-momentum dispersions[10–13] is an interesting theoretical problem and a matter for future studies.

Although the experiments discussed so far have been carried out on well-characterized SWNTs, the G′ effect can now be used to study different SWNT samples. Figure 5a relates to n doping with phosphorous. In both nitrogen- and phosphorous-doped samples, we see a similarly downshifted G'_D peak. Interestingly, increasing the level of phosphorous doping increases the intensity of the lower energy G'_D peak without changing its frequency (not shown), showing that the phenomenon here is local. By local, we mean the number of defect sites increases with doping level, thus increasing the G'_D intensity, but there is no correlation between defect sites, so that $\omega_{G'_D}$ does not change. For nitrogen doping, a different intensity behaviour is observed. A low level of nitrogen doping (up to 7% in weight) actually reduces the G'_D peak observed in pristine samples, and increases G'_D again for higher nitrogen concentrations (not shown). This result supports the hypothesis that nitrogen doping in small quantities induces higher nanotube crystallinity[7]. This different behaviour for nitrogen and phosphorous doping can be related to their ionic radius r as compared with carbon, where $r_N < r_C < r_P$. First-principles calculations indicate that phosphorous is incorporated substitutionally in the body of the tube, but this atom pops out of the tubular structure, whereas the nitrogen atoms remain in-plane[7,31].

Besides addressing the effect of intentional doping, we now analyse the G′ band in pristine samples prepared by the chemical vapour deposition (CVD) method without any nitrogen or phosphorous precursor (see Fig. 5b). Surprisingly, a small G'_D peak is observed in the as-grown sample (see down-arrow at the top spectrum of Fig. 5b). Although the defect structure here is unknown (some sort of doping, vacancy or other structural heterogeneity), the observation of the redshifted G'_D band indicates the presence of n-charged defects in the structure. It is interesting that, differently from the intentionally doped SWNT samples (with nitrogen or phosphorous), the G'_D peak in the pristine SWNTs disappears after annealing the sample at 200 °C in an argon flow, as shown in Fig. 5b. The n-type charged defects were present only before the annealing step.

The 'pristine' (before heat treatment, grown by arc-discharge or CVD), the nitrogen and the phosphorous SWNT doped samples all

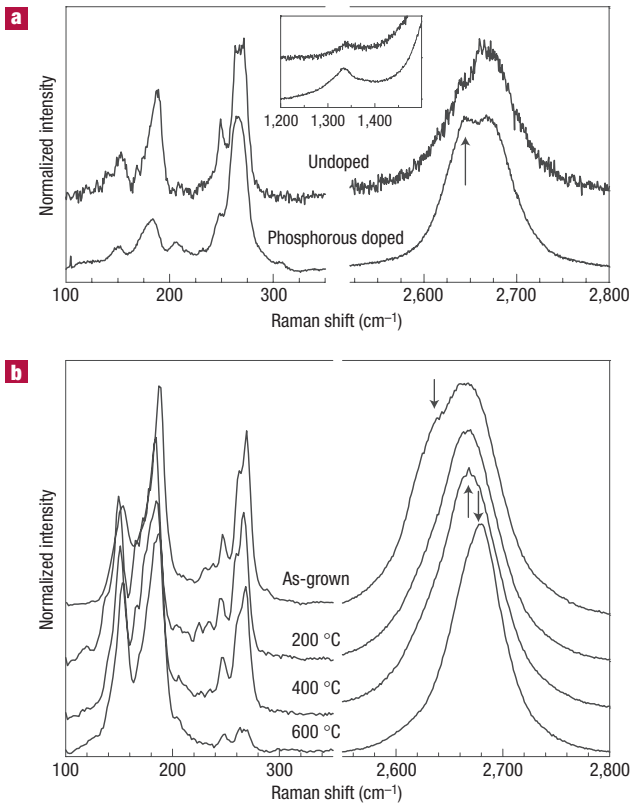

Figure 5 The use of the G′ feature to study doping in other SWNT samples. **a**, RBM (100–350 cm^{-1}) and G′ band (2,550–2,770 cm^{-1}) spectra for pristine and phosphorous-doped SWNTs after heat treatment. The RBM spectra are shown for monitoring the tube diameter (d_t) distribution ($\omega_{RBM} \propto 1/d_t$) (ref. 1). The arrow indicates the behaviour of the defect-induced G'_D peaks on doping. The inset shows the respective disorder-induced D band spectra[10–13] normalized to the G band (not shown). **b**, The effect of heat treatment on the RBM and G′ band spectra on pristine (unintentionally doped) CVD-grown SWNTs. The heat treatment temperatures are shown near the respective spectra. Annealing at 600 °C reduces the number of more reactive small-diameter tubes (larger ω_{RBM}—bottom spectrum in **b**), causing a shift in the G'_P band, in agreement with the diameter dependence of $\omega_{G'_P}$ (refs 21,22). The Raman spectra of the different SWNT samples were measured at room temperature with $E_{laser} = 2.41$ eV ($\lambda = 514$ nm). See Methods for sample details.

exhibit a lower frequency G'_D Raman peak with similar frequencies (see Supplementary Information for a comparative analysis), indicating that the electron and phonon renormalization near the defect site is caused by the presence of one extra electron. In the case of boron doping, the renormalization goes in the opposite direction, related to the presence of one hole. This extra electron/hole increases/decreases the electron speed locally, thus changing the atomic vibrations. The electron and phonon renormalization effects are not symmetric, being more pronounced for electron doping, in agreement with gate-induced doping experiments[24–26]. Our combined near-field photoluminescence and Raman data (Fig. 3) show that highly localized light emission is connected to a lower frequency G'_D, which results from n-type doping. Surprisingly this G′ defect-induced effect is common. It has been broadly observed in SWNTs (ref. 32) and in double-wall carbon nanotubes[33], although the underlying importance of defects in these structures has never been addressed. The multitude of samples exhibiting consistent results shows the generality of these findings. There exist other reports of localized optical emission from SWNTs (refs 20,34) and the physics discussed here will certainly apply to any other sp^2 carbon material[3,4,10,11].

The behaviour of the G'_D peak is, therefore, an effective probe to accurately measure the local effect of a single defect (including dopants) on the electronic and vibrational properties of carbon nanotubes, carbon nanoribbons, n-layer graphene or any other sp^2-hybridized carbon material. For quantitative doping level analysis, careful calibration studies have to be carried out, because the G′ intensity depends on tube diameter, metallicity and excitation laser energy[1]. Notice that the intensity of the defect-induced peak ($I_{G'_D}$) is higher than $I_{G'_P}$ for lower E_{laser} values, whereas $I_{G'_D}/I_{G'_P}$ goes to zero for higher E_{laser} values (see Fig. 4a). Figure 4c shows the intensity ratio $I_{G'_D}/I_{G'_P}$ as a function of E_{laser} (bottom axis) and the splitting between G'_P and G'_D (top axis). $I_{G'_D}$ is much less than $I_{G'_P}$ when $\omega_{G'_P} - \omega_{G'_D}$ is large. The ratio $I_{G'_D}/I_{G'_P}$ increases when the splitting gets smaller than the full-width at half-maximum of the G′ peaks ($\Gamma \sim 43$–53 cm^{-1}, see caption to Fig. 4) and the unperturbed and perturbed levels mix. The occupation of the defect-induced electronic states can be monitored from a G′ intensity analysis, shedding light on the field of excited electron dynamics[1,35].

METHODS

SAMPLE DETAILS

Nitrogen-doped SWNTs were grown by the CVD method at 950 °C using a solution of ethanol with 1.25% in weight of ferrocene and benzilamine in different concentrations (0%, 3.0%, 7.0% and 11.0% in weight) as a precursor carried by a 1.2 l min^{-1} flux of argon for 30 min. The diameter range is from 0.7 to 2.2 nm. The nitrogen content in the tubes has been evaluated by detailed X-ray photoelectron spectroscopy, resulting in 0.3 at.% incorporated in the nanotube lattice, regardless of the feedstock composition (Ayala *et al.*, manuscript in preparation). For this reason, most of the results discussed in our article, and shown in Figs 2 and 4, focus on the lowest initial content of benzilamine (3.0% in weight). The X-ray photoelectron spectroscopy results also indicate the nitrogen incorporates into the SWNT lattice in both the sp^2 substitutional and the pyridinic bonding.

Boron-doped SWNTs were grown by the pulsed laser vaporization technique using targets with three different boron concentrations, undoped, 1.5 at.% and 3.0 at.%. The laser ablation technique is known to generate relatively pure and high-quality nanotubes as compared with CVD samples, and the lower frequency (n-type related) G'_D peak is never observed, thus making it possible to unambiguously probe the p-doping behaviour. The diameter range of these samples varies with doping within the range of 1.1 to 1.7 nm. Clear evidence for substitutional boron doping into the SWNT lattice has been obtained from Raman spectroscopy, thermoelectric power, temperature-dependent magnetization measurements, electric and thermal transport[14,15] and most recently from nuclear magnetic resonance and Meissner effect experiments[36]. The amount of doping is small (less than 1 at.%). Furthermore, consistent with what is known about boron incorporation in graphite, addition of more than 3.0 at.% boron in the graphite target was found to inhibit the formation of SWNTs. Soot generated from targets containing 1.5 at.% boron gives the best doped SWNTs with respect to level of doping versus quality of tube structure[15]. For this reason, the sample we used to draw the conclusions in our article, and shown in Fig. 2, was the SWNTs grown in the 1.5 at.% boron-doping condition.

The CVD SWNTs doped with phosphorous were grown at 950 °C using a solution of ethanol with 1.25% in weight of ferrocene and triphenilphosphine in different concentrations (0%, 0.1%, 0.15%, 0.20% and 0.25% in weight) as a precursor carried by a 0.8 l min^{-1} flux of argon with 5% of hydrogen for 30 min. The spectrum shown in Fig. 5a is for the 0.20% concentration. The diameter range is from 0.7 to 2.2 nm. When compared with nitrogen and boron doping, phosphorous doping is still in the development stage. Phosphorous incorporation in multi-wall carbon nanotube lattices has already been demonstrated[31], and the result discussed in Fig. 5a provides an unprecedented indication for the incorporation of phosphorous into SWNT lattices.

Thermal treatments (shown in Fig. 5) were carried out in a 0.5 l min^{-1} argon flow to avoid tube oxidation, for 30 min at 200, 400 and 600 °C.

The SWNT samples used in the near-field measurements were produced by arc-discharge, dispersed in a solution of dichloroethane, sonicated in an ultrasonic bath and spin-cast at 3000 r.p.m. onto a glass coverslip. The sample was then inspected by confocal Raman scattering. The resulting images revealed isolated spots indicative of well-separated nanotubes. The observation of the localized G'_D peak, along with the bi-modal n/p-type-dependent G'_D behaviour in agreement with gate-induced doping experiments in carbon nanotubes[26], represents the initial motivation for this study.

The graphene sample was obtained by micromechanical cleavage of graphite on the surface of a Si sample with a 300 nm layer of SiO_2.

EXPERIMENTAL DETAILS

Far-field Raman measurements were carried out with a Dilor XY triple-monochromator equipped with a CCD (charged-coupled device) detector. The backscattering configuration using a ×80 objective and different excitation laser energies were used for resonance micro-Raman measurements. The excitation came from an ArKr laser ($E_{laser} = 1.91$, 2.18, 2.41 and 2.54 eV). Mapping of the RBM dependence on E_{laser} was carried out with a larger number of excitation energies, ranging from 1.61 to 2.71 eV (ArKr, Ti:sapphire and dye laser) for a precise characterization of the sample diameters.

Near-field Raman and near-field photoluminescence measurements were carried out on an inverted optical microscope with the addition of an x, y-stage for raster-scanning samples. Light from a He–Ne laser (633 nm) is reflected by means of a dichroic beam splitter and then focused onto the surface of the sample using a high numerical aperture objective (N.A. = 1.4), with 10^3 W cm^{-2} at the sample. Having obtained a tight focal spot at the sample surface, we then position a sharp metal tip into the focal region. Using the x, y-scan stage to raster-scan the sample, the Raman scattered light and photoluminescence are collected by the same microscope objective and recorded using either a single-photon counting avalanche photodiode or a spectrograph with a CCD cooled to −124 °C.

Received 28 February 2008; accepted 19 September 2008; published 19 October 2008.

References

1. Jorio, A., Dresselhaus, M. S. & Dresselhaus, G. *Carbon Nanotubes: Advanced Topics in the Synthesis, Structure, Properties and Applications* Vol. 111 (Springer Series in Topics in Appl. Phys., Springer, 2008).
2. Novoselov, K. S. *et al.* Two-dimensional gas of massless Dirac Fermions in graphene. *Nature* **438**, 197–200 (2005).
3. Piscanec, S., Lazzeri, M., Mauri, F., Ferrari, A. C. & Robertson, J. Kohn anomalies and electron–phonon interactions in graphite. *Phys. Rev. Lett.* **93**, 185503 (2004).
4. Ando, T. Anomaly of optical phonon in monolayer graphene. *J. Phys. Soc. Jpn.* **75**, 124701 (2006).
5. Tsang, J. C., Freitag, M., Perebeinos, V., Liu, J. & Avouris, P. Doping and phonon renormalization in carbon nanotubes. *Nature Nanotech.* **2**, 725–730 (2007).
6. Pisana, S. *et al.* Breakdown of the adiabatic Born–Oppenheimer approximation in graphene. *Nature Mater.* **6**, 198–201 (2007).
7. Terrones, M., Souza Filho, A. G. & Rao, A. M. *Doped Carbon Nanotubes: Synthesis, Characterization and Applications* Vol. 111, 531–566 (Springer Topics in Appl. Phys., Springer, 2008).
8. Jones, M. *et al.* Extrinsic and intrinsic effects on the excited-state kinetics of single-walled carbon nanotubes. *Nano Lett.* **7**, 300–306 (2007).
9. Cognet, L. *et al.* Stepwise quenching of exciton fluorescence in carbon nanotubes by single-molecule reactions. *Science* **316**, 1465–1468 (2007).
10. Ferrari, A. C. & Robertson, J. Raman spectroscopy in carbons: From nanotubes to diamond. *Phil. Trans. R. Soc. Lond. A* **362**, 2267–2565 (2004).
11. Pimenta, M. A. *et al.* Studying disorder in graphite-based systems by Raman spectroscopy. *Phys. Chem. Chem. Phys.* **9**, 1276–1291 (2007).
12. Thomsen, C. & Reich, S. Double resonant Raman scattering in graphite. *Phys. Rev. Lett.* **85**, 5214 (2000).
13. Saito, R. *et al.* Probing phonon dispersion relations of graphite by double resonance Raman scattering. *Phys. Rev. Lett.* **88**, 027401 (2002).
14. Rao, A. M., Eklund, P. C., Bandow, S., Thess, A. & Smalley, R. E. Evidence for charge transfer in doped carbon nanotube bundles from Raman scattering. *Nature* **388**, 257–259 (1997).
15. McGuire, K., Gothard, N., Gai, P. L., Dresselhaus, M. S., Sumanasekera, G. & Rao, A. M. Synthesis and Raman characterization of boron-doped single-walled carbon nanotubes. *Carbon* **43**, 219–227 (2005).
16. Villapando-Paez, F. *et al.* Synthesis and characterization of long strands of nitrogen-doped single-walled carbon nanotubes. *Chem. Phys. Lett.* **424**, 345–352 (2006).
17. Ferrari, A. C. *et al.* Raman spectrum of graphene and graphene layers. *Phys. Rev. Lett.* **97**, 187401 (2006).
18. Gupta, A., Chen, G., Joshi, P., Tadigadapa, S. & Eklund, P. C. Raman scattering from high-frequency phonons in supported *n*-graphene layer films. *Nano Lett.* **6**, 2667–2673 (2006).
19. Malard, L. M. *et al.* Probing the electronic structure of bilayer graphene by Raman scattering. *Phys. Rev. B* **76**, 201401 (2007).
20. Anderson, N., Hartschuh, A., Cronin, S. & Novotny, L. Nanoscale vibrational analysis of single-walled carbon nanotubes. *J. Am. Chem. Soc.* **127**, 2533–2537 (2005).
21. Dresselhaus, M. S., Dresselhaus, G., Saito, R. & Jorio, A. Raman spectroscopy of carbon nanotubes. *Phys. Rep.* **409**, 47–99 (2005).
22. Souza Filho, A. G. *et al.* Competing spring constant versus double resonance effects on the properties of dispersive modes in isolated single-wall carbon nanotubes. *Phys. Rev. B* **67**, 035427 (2003).
23. Samsonidze, Ge. G. *et al.* Phonon trigonal warping effect in graphite and carbon nanotubes. *Phys. Rev. Lett.* **90**, 027403 (2003).
24. Das, A. *et al.* Monitoring dopants by Raman scattering in an electrochemically top-gated graphene transistor. *Nature Nanotech.* **3**, 210–215 (2008).
25. Das, A. *et al.* Phonon renormalization in doped bilayer graphene, Preprint at <http://arxiv.org/abs/0807.1631> (2008).
26. Corio, P., Jorio, A., Demir, N. & Dresselhaus, M. S. Spectro-electrochemical studies of single wall carbon nanotubes films. *Chem. Phys. Lett.* **392**, 396–402 (2004).
27. Lazzeri, M., Attaccalite, C., Wirtz, L. & Mauri, F. Impact of the electron–electron correlation on phonon dispersions: Failure of LDA and GGA functionals in graphene and graphite. *Phys. Rev. B* **78**, 081406(R) (2008).
28. Peres, N. M. R. *et al.* Electron waves in chemically substituted graphene. *Europhys. Lett.* **80**, 67007 (2007).
29. Hwang, E. H., Hu, B. Y.-K. & Sarma, S. D. Density dependent exchange contribution to $\partial\eta/\partial n$ and compressibility in graphene. *Phys. Rev. Lett.* **99**, 226801 (2007).
30. Park, C.-H., Giustino, F., Cohen, M. L. & Louie, S. G. Velocity renormalization and carrier lifetime in graphene from the electron–phonon interaction. *Phys. Rev. Lett.* **99**, 086804 (2007).
31. Cruz-Silva, E. *et al.* Heterodoped nanotubes: Theory, synthesis, and characterization of phosphorus-nitrogen doped multiwalled carbon nanotubes. *Acs Nano.* **2**, 441–448 (2008).
32. Cardenas, J. F. & Gromov, A. Double resonance Raman scattering in solubilised single walled carbon nanotubes. *Chem. Phys. Lett.* **442**, 409–412 (2007).
33. Pfeiffer, R., Kuzmany, H., Simon, F., Bokova, S. N. & Obraztsova, E. Resonance Raman scattering from phonon overtones in double-wall carbon nanotubes. *Phys. Rev. B* **71**, 155409 (2005).
34. Freitag, M. *et al.* Scanning photovoltage microscopy of potential modulations in carbon nanotubes. *Appl. Phys. Lett.* **91**, 031101 (2007).
35. Perebeinos, V. & Avouris, Ph. Phonon and electronic nonradiative decay mechanisms of excitons in carbon nanotubes. *Phys. Rev. Lett.* **101**, 057401 (2008).
36. Murata, M. *et al.* Superconductivity in thin films of boron–doped carbon nanotubes. *Phys. Rev. Lett.* **101**, 027002 (2008).

Supplementary Information accompanies the paper at www.nature.com/naturematerials.

Acknowledgements

The authors acknowledge A. H. Castro-Neto, R. B. Capaz, J. Lefebvre and R. Dickman for helpful discussions. I.O.M., M.A.P. and A.J. acknowledge financial support from the *Rede Nacional de Pesquisa em Nanotubos de Carbono*, *Rede National de SPM*, *Instituto de Nanotecnologia* (MCT-CNPq) and CAPES/DAAD-Probral. A.H. and H.Q. acknowledge financial support from the Deutsche Forschungsgemeinschaft (Me 1600/6-1/2). M.T, H.T and J.C.D acknowledge financial support from CONACYT-Mexico Grants No.45762, 45772, 41464-Inter American Collaboration, 42428-Inter American Collaboration and PUE-2004-CO2-9 Fondo Mixto de Puebla. A.M.R acknowledges K. McGuire and financial support from NSF DMR 0304019. N.A. and L.N. acknowledge financial support from the DOE (grant DEFG02-05ER46207) and NSF (grant CHE-0454704).

Author contributions

Project planning: A.J.; sample preparation: I.O.M., N.A., M.T, H.T., J.C.D., A.M.R.; far-field measurements: I.O.M, M.A.P., A.J.; near-field measurements: N.A., A.H., H.Q., L.N., A.J.; all authors contributed to data analysis and scientific discussions.

Author information

Reprints and permissions information is available online at http://npg.nature.com/reprintsandpermissions. Correspondence and requests for materials should be addressed to L.N. or A.J.